Supplemental Material

Determination of the Vacancy Distribution over Al Cation Sites in γ-Al$_2$O$_3$

Henry O. Ayoola[a], Cheng-Han Li[b], Stephen D. House[a,c,d], Matthew P. McCann[a], Joshua J. Kas[e], Joerg Jinschek[b], John J. Rehr[e], Wissam A. Saidi[*f,g], Judith C. Yang[*a,c,h]

[a] Department of Chemical and Petroleum Engineering, University of Pittsburgh, Pittsburgh, PA 15261, USA
[b] Department of Materials Science and Engineering, The Ohio State University, Columbus, OH 43210, USA
[c] Environmental TEM Catalysis Consortium (ECC), University of Pittsburgh, Pittsburgh, PA 15261, USA
[d] Center for Integrated Nanotechnologies, Sandia National Laboratories, Albuquerque, NM 87123, USA
[e] Department of Physics, University of Washington, Seattle, WA 98195, USA
[f] Department of Mechanical Engineering and Materials Science, University of Pittsburgh, Pittsburgh, PA 15261, USA
[f] National Energy Technology Laboratory, Pittsburgh, PA 15236, USA
[h] Department of Physics and Astronomy, University of Pittsburgh, Pittsburgh, PA 15261, USA

*Corresponding author: alsaidi@pitt.edu; judyyang@pitt.edu

Sample preparation

Bulk NiAl was cut into 5 mm x 5 mm x 1 mm pieces and mechanically polished with sequentially finer SiC polishing papers from 30 μm to 0.05 μm grit. The sample was then cleaned with Ar plasma for 10 minutes. The polished and cleaned NiAl was oxidized in a conventional tube furnace at 850 °C for 1 hour yielding an ~80 nm thick single crystal (111) aluminum oxide film. The sample was then allowed to cool slowly to room temperature overnight, to minimize residual strain due to coefficient of thermal expansion (CTE) mismatch. Cross-sectional transmission electron microscopy (TEM) samples were prepared using an FEI Scios (dual beam) focused ion beam (FIB) at 30 kV and 5 kV as final polishing step. TEM images and SAED patterns were acquired with a Hitachi H9500 TEM at 300 kV. The monochromated EELS spectra were acquired on an FEI Titan3™ G2 operated at 300 kV with a Gatan Image Filter. The sample was placed in a Gatan Ultra Low Temperature Double-Tilt (ULTDT) cryo-holder maintained at liquid nitrogen temperature (range: -170 to -190 °C) during EELS experiments to minimize electron beam damage.

Simulation procedure

Calculation of the energy-loss near-edge spectra (ELNES) for the various γ-Al$_2$O$_3$ structures were carried out with the FEFF9 code. The O K and Al L$_{2,3}$ edges were calculated. The code calculates the ELNES spectrum for an individual selected atom, so the spectra for nonequivalent atom positions were calculated and averaged to generate the simulated spectra. The spectra are automatically aligned by FEFF, which gives an approximate chemical shift, as it is an all electron code. A single overall shift of the final averaged spectrum is used to align with experiment. Calculated ELNES spectra are aligned to the edge onset of the experimental spectra, after the experimental spectra have been aligned using the zero-loss peak.
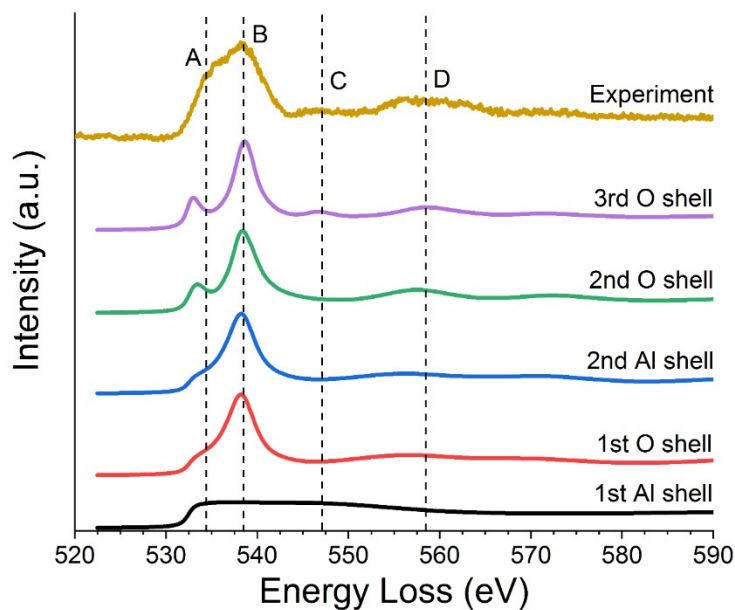
Spectra convergence with cluster size

Figure S1. Calculations of O-K edge ELNES for different cluster sizes surrounding the excited atom using the cubic spinel γ-Al$_2$O$_3$ model.

Figure S1 shows the O-K edge ELNES simulations of varying cluster sizes of the cubic spinel γ-Al$_2$O$_3$ model. The first Al shell produces no fine structure, with only the hydrogenic edge being produced. Overall, the shell-by-shell simulations show that the spectral features arise primarily from scattering from oxygen shells. This makes sense since O is a much stronger electron scatterer than Al [1-3]. The scattering from the 1st O shell produces the main peaks labeled B and D, scattering from the 2nd O shell produces the peak/shoulder A and scattering from the 3rd O

shell produces the subtle peak C. Thus, a basic representation of the O-K edge could be reproduced using a four-oxygen-shell cluster (~6 Å cluster).

Spinel model simulations

For each vacancy configuration, a large supercell of the spinel structure was made with no vacancies, then Al atoms were randomly removed to get the correct percentage of tetrahedral/octahedral vacancies. This created a large supercell with a central (primitive) cell which was used to calculate the EELS. This vacancy-doped supercell was then produced multiple times in order to perform configuration averaging of the EELS. FEFF is a cluster code, which is why a large supercell was used, but EELS was only calculated for the atoms in the central (primitive) cell in order to simulate the bulk properties. Self-consistent field potentials (SCF) were used with an SCF radius of 6 Angstroms (85–110 atoms) about the absorbing atom [A. L. Ankudinov, et al., Phys. Rev. B 58, 7565 (1998)], while the spectra were calculated using a full multiple scattering (FMS) radius of 8 Angstroms (224 atoms). These radii were sufficient to provide converged calculations of the final averaged spectrum. Averaging was performed over 30 separate configurations. Final state effects were included via the final-state rule core-hole, and the many-pole model self-energy [J.J.Kas et al., Phys. Rev. B 76, 195116 (2007)].

Limitations of the simulation procedure

FEFF uses the spherical muffin-tin approximation and does not perform calculations with full potentials. The spherical muffin-tin approximation for atomic potential fields approximates the potential field around atoms in a crystal lattice as non-overlapping spheres. The screened potential experienced by electrons within the sphere is approximated as spherically symmetric about the nucleus of the atom. This makes solutions to multiple-scattering equations more stable and easier to compute, but may also alter relative peak size especially as full potential effects can be large for d-states and can cause additional splitting of levels.

The approximate nature of many-body effects such as quasiparticle self-energy corrections, core-hole, and disorder-induced broadening in the FEFF calculations contribute to the slight difference in peak positions between the simulated spectra and the experimental spectrum.

Influence of strain on EELS spectra

Strain in the crystal lattice can influence the EELS spectra acquired from a sample [32]. In the case of crystalline Al_2O_3 grown by oxidation of NiAl, it is known that there is residual strain in the Al_2O_3 due to lattice and coefficient of thermal expansion (CTE) mismatch [33]. However, for the epitaxial growth of our samples, the degree of lattice mismatch between NiAl (002) and γ-Al_2O_3 (044) is 2.6%, which is small.

On the other hand, strain is detected in EELS spectra by small peak shifts in low-loss EELS spectra (on the order of 0.16 eV per 1% volume change). This effect is attributed to the

dependence of the valence electron density on the lattice parameter [32]. This effect is not expected to be replicated to the same degree in core-loss spectra, as electrons are being excited from inner shells into unoccupied states above the Fermi level, and not from or into the valence band. Since the effect of strain is small, and our analysis is focused on near-edge features and not absolute peak positions of the EELS edges, we used the optimized structures with no strain in our calculations.

To further verify this assumption, single site O K edge EELS simulations were done for the pristine monoclinic model and for the monoclinic model with lattice parameter **a** modified to simulate the lattice mismatch induced strain from the NiAl substrate. Figure S2 show that the spectra are nearly identical, validating our assumption that the effect of strain on the EELS spectra is negligible for the purposes of our study. Note that these are single O atom simulations; the necessary site-averaging done in the full simulations will broaden the peak features that differ between the spectra.
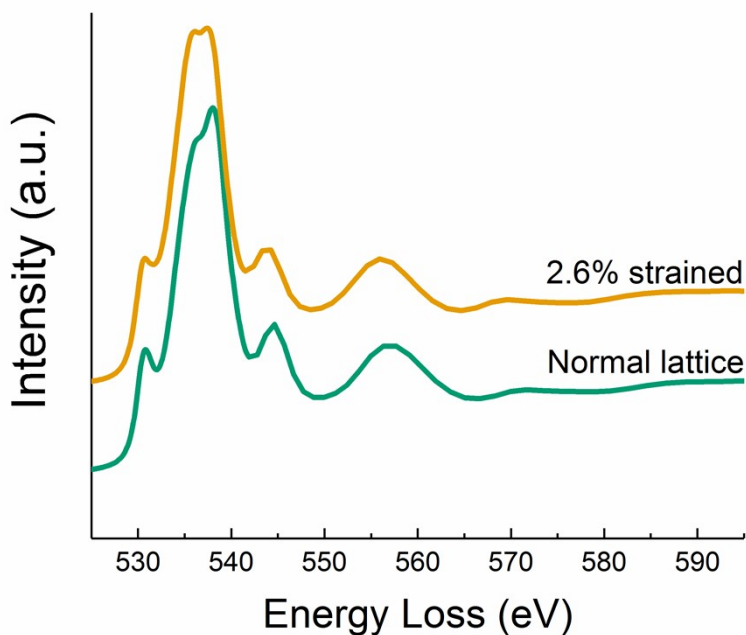

Figure S2. Simulated O K edge EELS spectra for a single central O atom in a cluster assembled using the normal monoclinic model lattice and a cluster simulating the lattice mismatch strain of the system. The near-identical spectra indicate that the impact of strain in our calculations is negligible.

Procedure to calculate mean absolute deviations for each vacancy distribution model

1. Calculate experimental intensity ratios

Integrated intensity was first calculated for each spot. First, a threshold mask was applied to the experimental diffraction pattern to exclude all pixels with intensity below 2x the background (Figure S3).
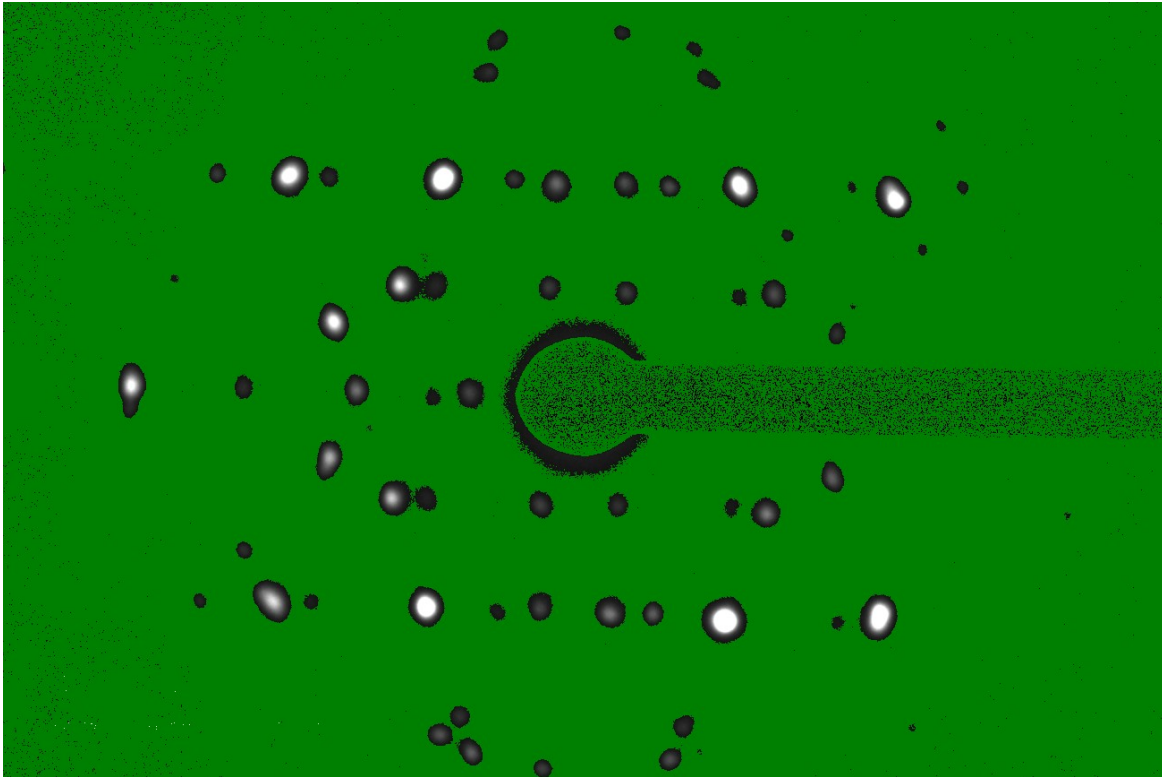

Figure S3. Experimental (110) zone axis SAED pattern with threshold mask applied. All pixels below the threshold are colored green.

Line profiles were placed on the diffraction spots to include the pixels above the threshold value. This produced a 2D Gaussian-like intensity profile for each spot. The profile for each spot was fit with a Gaussian and the area under the Gaussian was calculated (Figure S4). This provided the value for integrated intensity for that spot. The spot with the maximum integrated intensity among all symmetrically equivalent spots (e.g. spot D among all {440} spots appearing on the SAED pattern) was used as the intensity value for the given reflection.
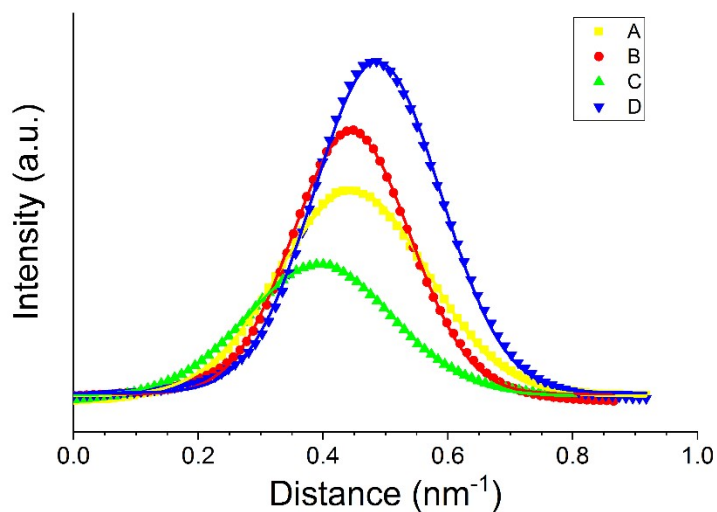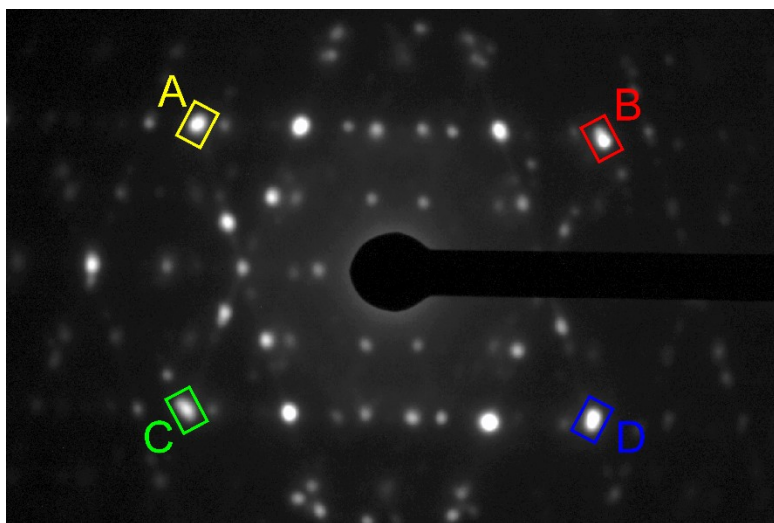
Figure S4. Example of line profiles taken of {440} spots from the [110] ZA SAED pattern. $R^2 >$ 0.95 for all Gaussian fits.

The intensity ratios were then calculated for the given pairs of reflections in Table 1 in the main text using the intensity for each reflection calculated above. This was done for each of the diffraction patterns, with the twin patterns counting as two separate patterns. The intensity ratios for the same reflection pair but from different patterns were then averaged to get the values shown in Table 1. The weighting given to each reflection pair was calculated by giving the brightest reflection, the {400} reflection, a value of 1 and scaling all the reflections appropriately. The weighting for each reflection pair was then calculated by averaging the weights for the two reflections and scaling to the sum of all the weights.

2. Calculate simulated intensity ratios for vacancy distribution models

Starting with the description of lattice parameters and atomic positions obtained from the Gutierrez cubic spinel-based model, models with varying Al vacancy distributions were made by altering the occupancy of tetrahedral (8a) and octahedral (16d) sites (Table S1). For each model, the diffraction data (i.e. list of reflections and their relative intensities) was calculated using SingleCrystal. The intensity ratios for the same pairs of reflections calculated for the experimental SAED patterns (as in Table 1 in the main text) were then calculated using the simulated diffraction data.

Table S1. Tetrahedral and octahedral site occupancy for all cubic spinel-based models used for SAED simulations.

Model	Fraction of vacancies in tetrahedral sites	Tetrahedral (8a) site occupancy	Octahedral (16d) site occupancy
1	0	1	0.8333
2	0.1	0.9667	0.8500
3	0.2	0.9333	0.8667
4	0.3	0.9000	0.8833
5	0.4	0.8667	0.9000
6	0.5	0.8333	0.9167
7	0.6	0.8000	0.9333
8	0.7	0.7667	0.9500
9	0.8	0.7333	0.9667
10	0.9	0.7000	0.9833
11	1	0.6667	1

Table S2. Example of intensity ratios calculated for a cubic spinel-based model with 50% (0.5) of Al vacancies placed on tetrahedral sites. The absolute deviation was calculated relative to the experimental intensity ratio values. The unweighted mean absolute deviation (MAD) for this model was calculated as 1.40. The weighted MAD was calculated as 1.93.

Reflections	Experimental intensity ratio	50% of Al vacancies on tetrahedral sites		Weighting
		Calculated intensity ratio	Absolute deviation ($|I_{exp}-I_{calc}|$)	
220/111	0.88	1.78	0.90	0.052
113/111	3.34	3.70	0.37	0.123
222/111	1.80	0.93	0.87	0.067
400/111	14.32	15.59	1.26	0.407
440/111	9.49	14.38	4.89	0.241
115/111	1.01	1.83	0.82	0.053
622/111	1.14	0.47	0.66	0.056

For each intensity ratio, the absolute deviation was calculated relative to the experimental value. An example of this process is shown in Table S2. The absolute deviations of the intensity ratios for all the considered models are shown in Figure S5. The absolute deviations for each reflection pair were then averaged to get the mean absolute deviation (MAD) which was used to compare the models to each other to determine the best fitting model.
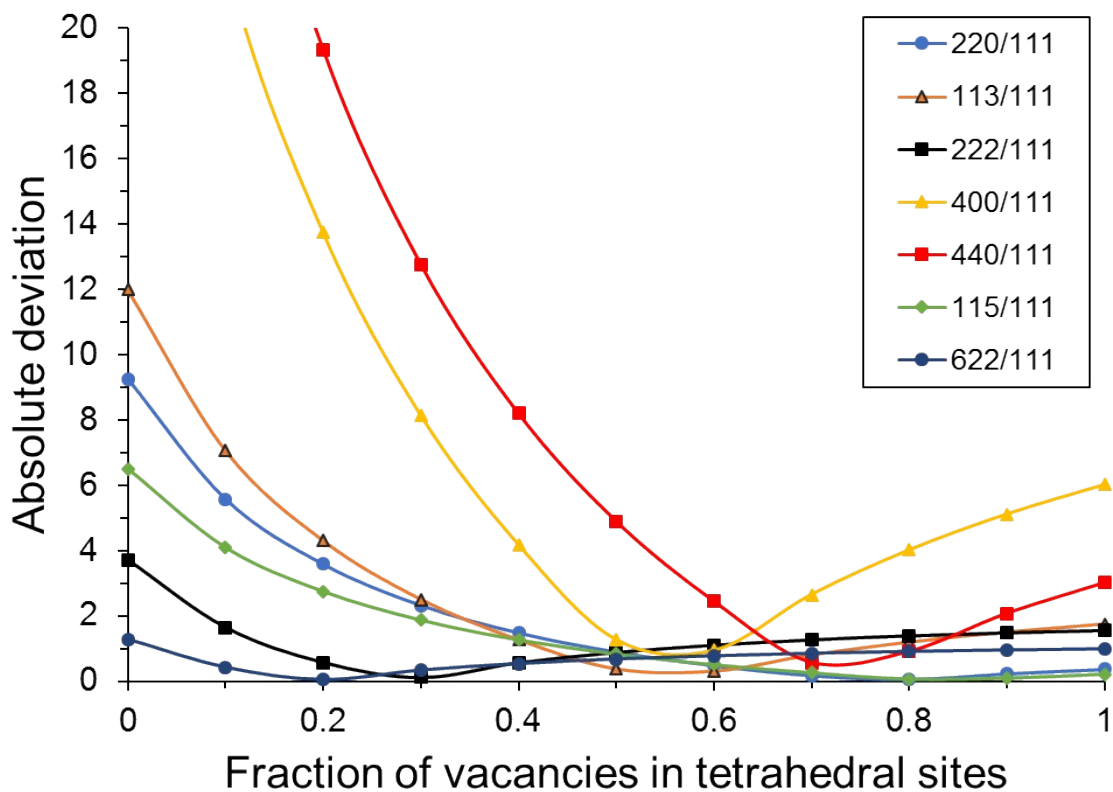
Figure S5. Absolute deviations of each intensity ratio relative to experimental value, plotted for each vacancy distribution model.

3. <u>Mean absolute deviation calculations (unweighted vs weighted)</u>

The plot of mean absolute deviation shown in Figure 1 in the main text is the weighted mean. An unweighted mean absolute deviation was also calculated. The unweighted MADs are shown in Figure S6. No significant difference is observable.
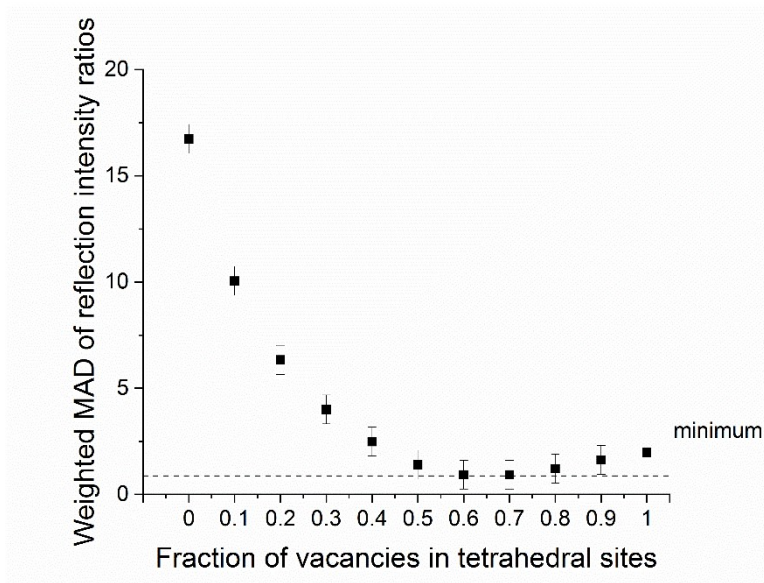
Figure S6. Unweighted mean absolute deviation (MAD) of reflection intensity ratios relative to the experimental values for each cubic spinel model vs fraction of Al vacancies in tetrahedral sites in the model.

Another set of calculations using another set of intensity ratios was performed to compare the effect of selecting different reflection pairs. The selected reflection pairs are shown in Table S2. The change in selection of reflection pairs had no significant effect on the calculated MAD values (Figure S7).

Table S3. Ratios of intensity of second set of reflection pairs.

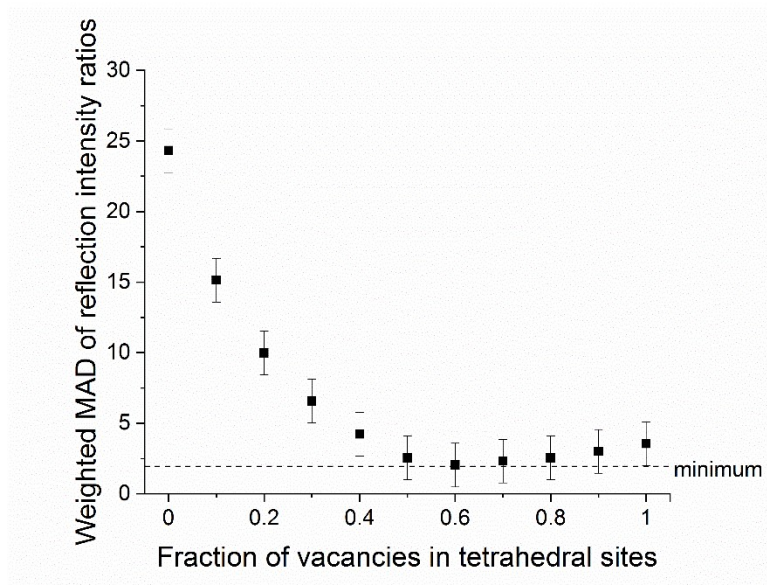| Reflections	Intensity ratios	Weighting
113/111	3.64 ± 0.02	0.102
113/220	3.98 ± 0.70	0.101
222/111	1.52 ± 0.17	0.055
400/111	14.32 ± 2.19	0.336
440/111	8.08 ± 1.91	0.199
113/115	3.63 ± 0.09	0.102
113/622	3.34 ± 0.20	0.104

Figure S7. Weighted mean absolute deviation (MAD) values for each cubic spinel model calculated using the data in Table S3.
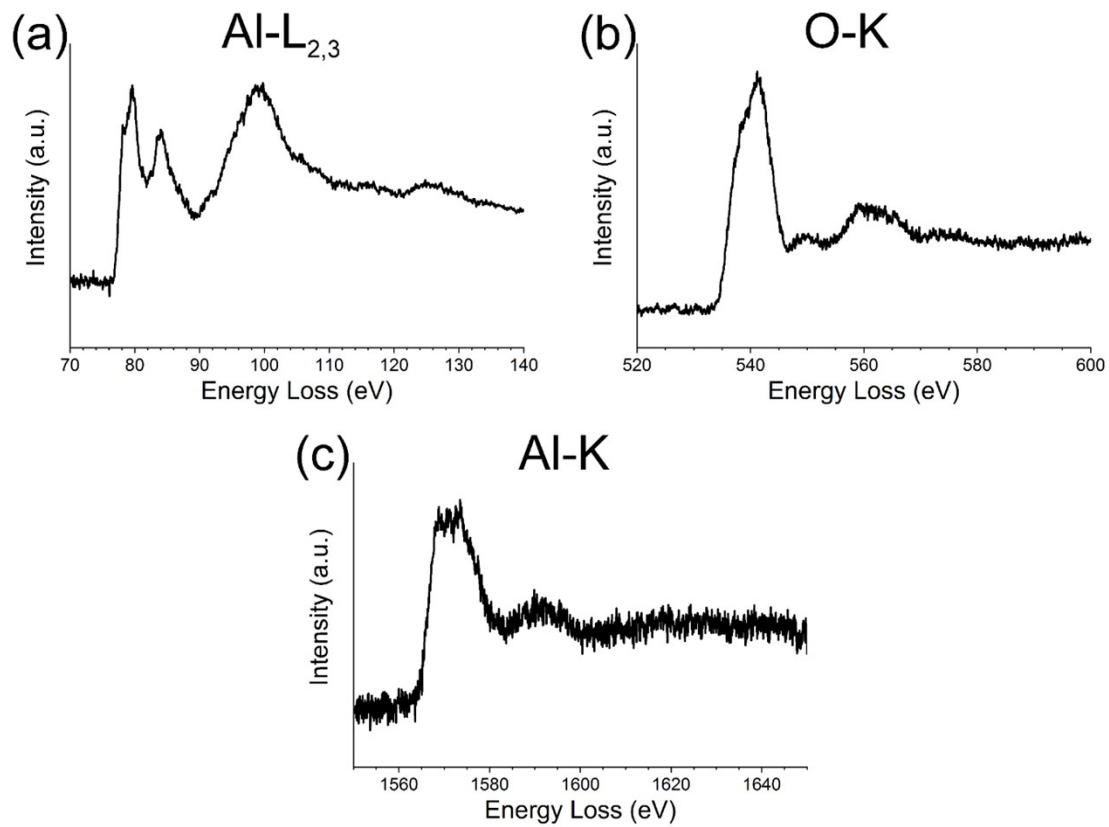
Experimental High-Resolution EELS spectra

Figure S8. (a) Al-L$_{2,3}$ edge, (b) O-K edge, and (c) Al-K edge EELS spectra acquired from γ-Al$_2$O$_3$.

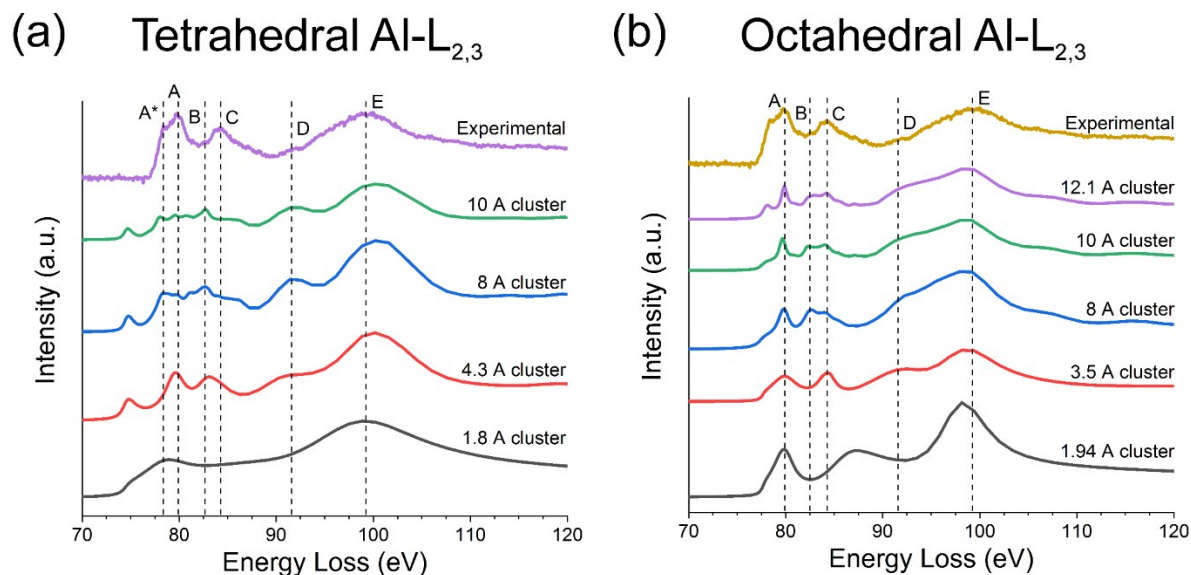**Tetrahedral Al vs Octahedral Al L$_{2,3}$ edge simulations**

Figure S9. Calculations of Al-L$_{2,3}$ edge ELNES for different cluster sizes surrounding a (a) tetrahedral and (b) octahedral excited Al atom using the cubic spinel γ-Al$_2$O$_3$ model.

Al-L$_{2,3}$ edge ELNES simulations of varying cluster sizes of the cubic spinel γ-Al$_2$O$_3$ model are shown in Figure S9. Figure S9a shows the calculations with a tetrahedral Al atom as the absorbing atom, whereas Figure S9b shows the calculations with an octahedral Al atom as the absorbing atom. In both cases, the peak labeled E is present throughout, including in the first shell calculations, indicating that this feature is a consequence of the scattering from the first tetrahedron or octahedron.

For the tetrahedral Al atom (Figure S9a), a significant degree of fine structure emerges as the cluster size is increased. This indicates that the tetrahedral Al-L$_{2,3}$ ELNES is sensitive to medium-range order and calculations should be done using as large a cluster as possible. Overall, the tetrahedral Al-L$_{2,3}$ edge ELNES does not appear to match the experimental EELS closely. This could either indicate a problem with the simulation of the tetrahedral Al-L$_{2,3}$ ELNES, or that the contribution of the tetrahedral Al to the overall γ-Al$_2$O$_3$ Al-L$_{2,3}$ edge EELS is minimal. To determine whether the former was the case, the Al-L$_{2,3}$ ELNES of berlinite (AlPO$_4$) was calculated and compared to the corresponding Al-L$_{2,3}$ edge EELS from literature [4] (Figure S10b) to gauge the accuracy of the FEFF simulation from tetrahedral Al atoms. AlPO$_4$ consists solely of tetrahedrally-coordinated Al atoms and should provide a baseline for scrutiny of the accuracy of the MS simulation. The Al-L$_{2,3}$ edge simulated from AlPO$_4$ did not exhibit a good match to the experimental spectrum. One potential explanation is that the relaxation of the dipole-selection rules governing the electronic transitions—required to accurately model the scattering from a non-centrosymmetric atom such as a tetrahedral Al atom—is not effectively accounted for in the FEFF calculations.

For the octahedral Al atom (Figure S9b), the main features (A,C-E) of the ELNES already appear with a 3.5 Å cluster, which corresponds to the 3rd oxygen shell about the central Al atom. However, some fine structure does develop with further increasing cluster sizes. The octahedral Al-L$_{2,3}$ edge ELNES exhibits a much better match to the experimental EELS. This suggests that there are significantly more octahedral Al atoms than tetrahedral in the γ-Al$_2$O$_3$ structure, which is expected. The accuracy of FEFF simulation of the Al-L$_{2,3}$ ELNES from an octahedral Al was also checked using alpha-alumina (α-Al$_2$O$_3$) which contains only octahedrally-coordinated Al atoms and displayed in Figure S10a. The simulation shows a much better match than the AlPO$_4$ Al-L$_{2,3}$ simulation. This further confirms the hypothesis that the non-centrosymmetric tetrahedral Al atom is the source of difficulty for the multiple scattering simulations using FEFF, since the octahedral Al—which is centrosymmetric—presents no significant issue.

FEFF uses the muffin-tin approximation, which approximates the potential field around atoms in a crystal lattice as spheres within which the potential experienced by electrons is symmetric about the nucleus of the atom, and the potential between the spheres as constant. This approximation can have a significant effect on d-state level splitting [5].
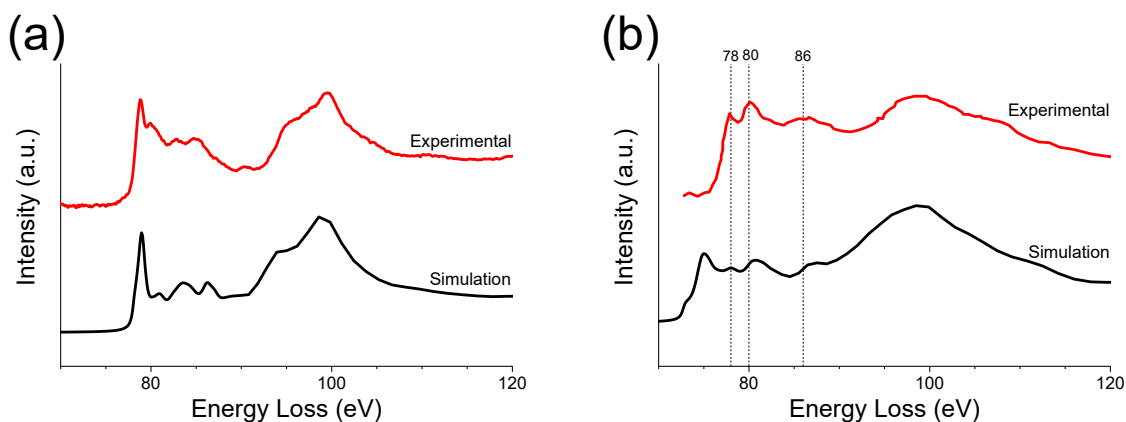

Figure S10. Al-L$_{2,3}$ EELS simulations from (a) alpha-alumina (α-Al$_2$O$_3$) and (b) berlinite (AlPO$_4$) compared to experimental EELS [4] showing the better agreement of the octahedral Al simulated EELS in (a) to experiment than the tetrahedral Al simulated EELS.
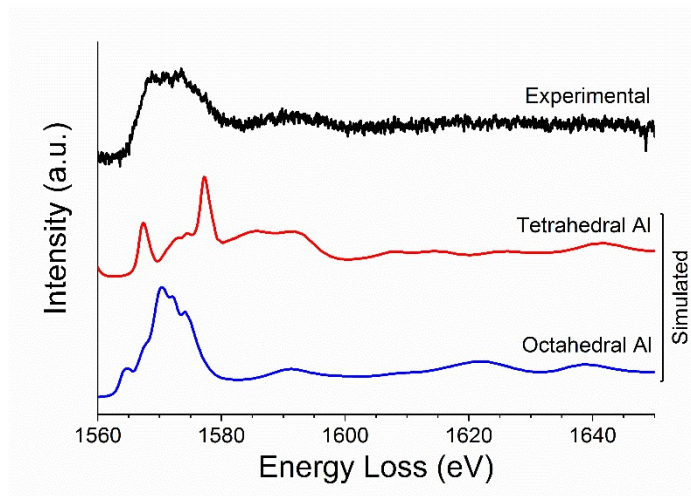
Figure S11. Simulated Al-K edge ELNES for both a single tetrahedral Al atom and a single octahedral Al atom in the cubic-spinel based model compared to the experimental Al-K edge spectrum.
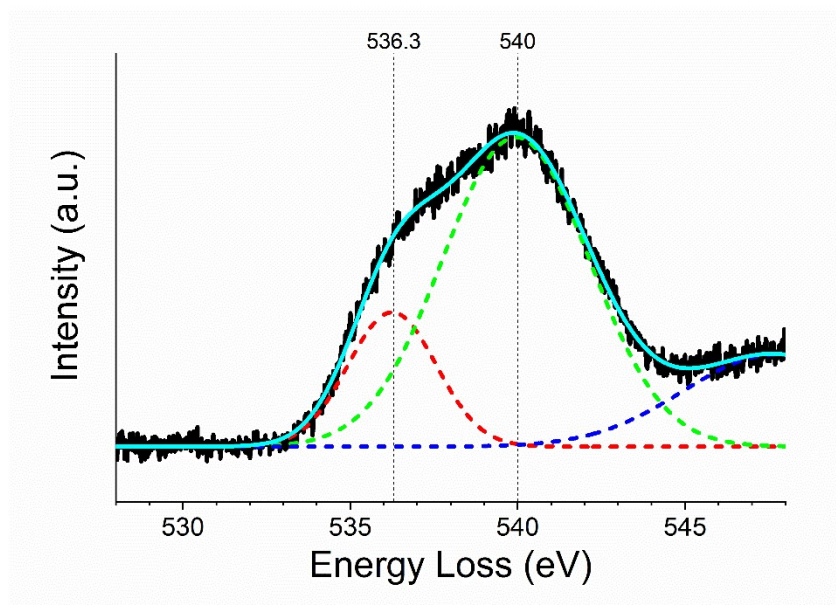

Figure S12. Fitting the O-K edge broad peak (labeled A in main document) with two Gaussian peaks. An excellent fit was achieved with $R^2 = 0.99$ with the peak positions and widths plotted in dashed lines.

References

1. Kurata, H., et al., *Electron-energy-loss near-edge structures in the oxygen K-edge spectra of transition-metal oxides.* Physical Review B, 1993. **47**(20): p. 13763-13768.
2. Brydson, R., *Multiple scattering theory applied to ELNES of interfaces.* Journal of Physics D: Applied Physics, 1996. **29**(7): p. 1699-1708.
3. Hansen, P.L., et al., *EELS fingerprint of Al-coordination in silicates.* Microsc. Microanal. Microstruct., 1994. **5**(3): p. 173-182.
4. Bouchet, D. and C. Colliex, *Experimental study of ELNES at grain boundaries in alumina: intergranular radiation damage effects on Al-L23 and O-K edges.* Ultramicroscopy, 2003. **96**(2): p. 139-152.
5. van Benthem, K. and H. Kohl, *Methods for ELNES-quantification: characterization of the degree of inversion of Mg–Al-spinels.* Micron, 2000. **31**(4): p. 347-354.